Dopant redistribution and electrical activation in silicon following ultra-low energy boron implantation and excimer laser annealing

S. Whelan,* A. La Magna, V. Privitera, G. Mannino, M. Italia, and C. Bongiorno
CNR-IMM, Stradale Primosole 50, 95121 Catania, Italy

G. Fortunato and L. Mariucci
CNR-IFN, Via Cineto Romano 42, 00156 Rome, Italy

(Received 6 May 2002; revised manuscript received 4 November 2002; published 5 February 2003)

Excimer laser annealing (ELA) of ultra-low-energy (ULE) B-ion implanted Si has been performed. High-resolution transmission electron microscopy has been used to assess the as-implanted damage and the crystal recovery following ELA. The electrical activation and redistribution of B in Si during ELA has been investigated as a function of the laser energy density (melted depth), the implant dose, and the number of laser pulses (melt time). The activated and retained dose has been evaluated with spreading resistance profiling and secondary ion mass spectrometry. A significant amount of the implanted dopant was lost from the sample during ELA. However, the dopant that was retained in crystal material was fully activated following rapid resolidification. At an atomic concentration below the thermodynamic limit, the activation efficiency (dose activated/dose implanted into Si material) was a constant for a fixed melt depth, irrespective of the dose implanted and hence the total activated dose was raised as the implant dose was increased. The electrical activation was increased for high laser energy density annealing when the dopant was redistributed over a deeper range.

DOI: 10.1103/PhysRevB.67.075201 PACS number(s): 61.72.Tt, 61.80.Ba, 61.82.Fk, 66.10.Cb

I. INTRODUCTION

Ultrashallow, electrically activated layers can be formed in Si through a combined process of ultra-low-energy (ULE) ion implantation and high ramp rate (400 °C/s), short time (<1 s), high temperature (>1000 °C), ''spike'' annealing.[1] Although the ions are implanted at low energy and their range in the solid is very shallow, radiation damage is formed in Si.[2] High-temperature annealing is required in order to activate a sufficient fraction of the implanted dopant and to dissociate the most complex defects that evolve from the as-implanted radiation damage. It is during high-temperature annealing that transient enhanced diffusion[3] of the dopant occurs, resulting in a redistribution of the dopant over depths much deeper than expected for thermal equilibrium diffusion. Optimizations of thermal processes such as the anneal ambient, ramp rate, and anneal time have been achieved so that ultrashallow junctions (95 nm) with a low sheet resistance ($Rs = 306\ \Omega/\mathrm{sq}$) (Ref. 1) can now be formed. However, as radiation damage is always formed in Si during ULE ion implantation, the dissociation of defects during the activation process step will inherently lead to an increase in the junction depth, and will ultimately impose a lower limit on the obtainable junction depth achievable through ion implantation and ''conventional'' thermal processing.

Excimer laser annealing[4] (ELA) of ion-implanted Si has received renewed interest within the semiconductor community recently for its possible application to the formation of ultrashallow junctions in Si. The technique offers many advantages compared to rapid thermal annealing (RTA) procedures, such as control over the junction depth and a higher dopant activation efficiency.[5] When irradiating Si with laser light at a sufficient energy density, a melted zone is formed[6] in the material. As the pulse is highly monoenergetic, the melted zone is well defined and a sharp transition between liquid the solid phase is formed. The diffusivity of B is raised in the liquid state ($\sim 10^{-4}$ cm^2/s),[7] and the dopant is able to redistribute uniformly within the melted layer. Due to the steep thermal gradient between the liquid and solid phases, immediately after irradiation the liquid-crystal interface advances toward the surface at a rate of $\sim$5 m/s.[8] As a result of such rapid solidification (the low-temperature solid phase regrowth is typically 1.5×10^{-10} m/s at 550 °C), less dopant is segregated into the liquid phase at the liquid-crystal interface and enhanced dopant trapping occurs.

The fraction of the implant dose which is retained within the semiconductor during ELA is governed by segregation (during regrowth), evaporation (during the melted phase), and ablation (during energy deposition). The electrical activation of the retained dopant in the regrown layer following ELA is limited by morphological instability at the liquid-crystal interface during regrowth,[9] lattice strain,[10] and the thermodynamic limit.[11] Interface instability may develop during regrowth when the concentration of the rejected dopant into the liquid phase during regrowth is high. Interface instability results in crystal irregularity (cell formation) in the surface region and the dopant retained within this region will remain electrically inactive. If laser annealing conditions permit, the maximum solubility of B in Si is ultimately governed by the lattice strain. Lattice strain is caused by the high substitutional fraction of the small covalent radius B atom in the Si lattice, and occurs when the atomic concentration exceeds 5 at % and the regrowth velocity is high. Under such conditions, the strained layer relaxes after regrowth and cracks are formed in the crystal lattice. Such crystalline defects reduce or inhibit the electrical activation of the retained dopant. At regrowth velocities and dopant concentrations when strain does not limit the B substitutional concentration, the maximum level of solute trapping is reached at the ther-

modynamic limit. The thermodynamic limit is governed by the regrowth velocity and the dopant diffusivity in the liquid state, and imposes an upper limit upon the level of solute trapping that can be achieved from the liquid state for a given dopant concentration.

Inactive dopant may remain in the solid following interface instability and strained-layer relaxation. When the thermodynamic limit is reached segregation occurs, and the dopant retained in the solid is expected to be fully activated (unless interface instability occurs). Although the junction depth can be easily defined when using ELA for the formation of shallow junctions in Si, a suitable choice of the laser anneal condition and the implanted dose is required in order to activate and retain a sufficient fraction of the implant dopant.

The radiation damage caused by low-energy B-ion implantation and the crystal recovery following an ELA process step have been assessed with high resolution transmission electron microscopy (HRTEM). The issues associated with dopant activation in Si following ELA have been addressed in this paper. Spreading resistance profiling (SRP) in combination with secondary ion mass spectrometry (SIMS) has enabled an assessment of the active and retained dose to be made. The dopant activation and dopant loss has been investigated as a function of the melt depth, the implant dose, and the melt time. A simulation model considering the dopant redistribution that occurs during melting and regrowth has been developed and compared to the experimental results.

II. EXPERIMENT

Boron was implanted into Si (100) (7° tilt, 30° twist angles) at an energy of 1 keV. The dopant was implanted at doses of 1×10^{14}, 1×10^{15}, and 5×10^{15} ions/cm^2. Post-implantation laser annealing was performed using a Lambda Physik LPX 205 XeCl excimer laser ($\lambda=308$ nm, 28-ns pulse duration), equipped with a beam homogeniser, which formed a uniform 7×7-mm^2 spot on the sample. The ELA process was performed in vacuum with the sample temperature maintained at 450 °C during irradiation.

The dopant activation as a function of depth was measured with SRP. In order to achieve accurate ultrashallow profiles, special procedures of probe conditioning and sample preparation[12] were followed. Moreover, the bevel edge effect,[13] a severe artifact at the case of shallow junctions, has been taken into account. In order to confirm SRP measurements after the bevel edge correction, the sheet resistance of the activated shallow layer was measured with a four-point probe (FPP). Prior to FPP measurements the samples were subjected to a HF dip so as to remove the surface oxide layer and to ensure a good contact between the probes and the sample surface during measurement. After consideration of the bevel edge effect, the sheet resistance measured with the four-point probe matched the value calculated with SRP. A SIMS analysis was performed with an IMS-Cameca instrument upon selected samples in order to obtain an indication of the chemical atomic concentration formed in the solid after ELA. Energetic Cs ions have been used to induce atomic sputtering. The ion energy upon leaving the source was at 7.5 keV, and with the target held at 4.5 keV, resulted in an ion impact energy of 3 keV. The sputtering rate during analysis was assumed constant when converting the crater depth into a depth scale. HRTEM structural analysis has been performed upon an as-implanted and a selected sample after ELA. HRTEM enabled lattice imaging of the near surface regions (<100 Å) with the (200 keV) electron beam parallel to the [110] direction of the crystalline substrate.

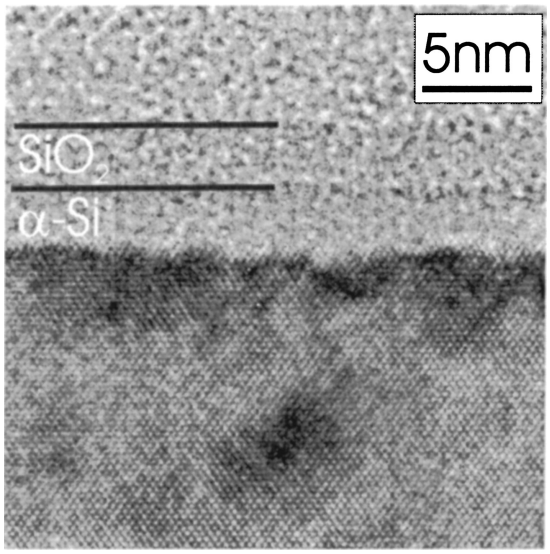

FIG. 1. HRTEM of the as-implanted damage structure formed in Si after 1-keV B implantation to a dose of 1×10^{15} ions/cm^2.

III. RESULTS

An *n*-type Si wafer implanted with 1-keV B to a dose of 1×10^{15} ions/cm^2 has been analyzed with HRTEM prior to laser annealing. A high-resolution image taken from the as-implanted sample (Fig. 1), shows that a subsurface amorphous layer resides under the surface oxide layer (~3 nm), which extends to a depth of ~3 nm into the substrate. The mean projected range, as calculated with TRIM,[14] for 1-keV B in Si (with an oxide considered), is 5.2 nm, which corresponds to the transition position from amorphous Si to damaged crystal. The interface between amorphous and damaged crystal material is not well defined and it can be seen that immediately below the amorphous layer there is considerable distortion in the lattice caused by the uptake of nonsubstitutional B. The distortion is likely to be direct evidence of a highly defect populated region. The as-implanted SIMS profile for a 1-keV B implant is presented in Fig. 2. It can be seen that for 1-keV B implantation, 80% of the retained B is contained within the first 10 nm of the sample. It is also important to note that at such low energy, a fraction (10%) of the implanted dopant remains in the native oxide layer prior to annealing.

A. Laser beam processes

Figure 3 shows the relationship between the calculated melt depth in crystal Si (maintained at 450 °C) vs the laser

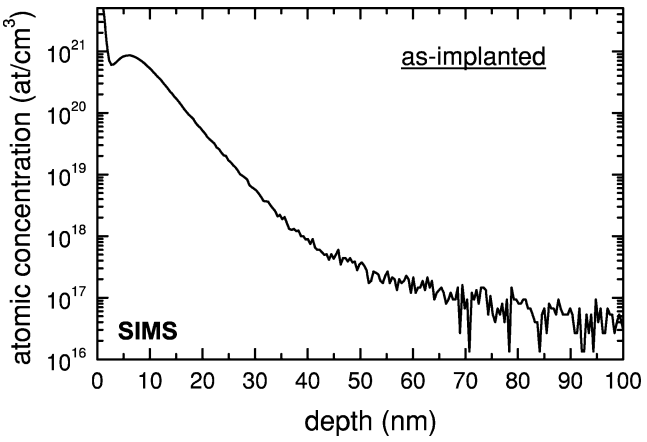

FIG. 2. SIMS dopant profile taken from a sample implanted with 1-keV B to a dose of 1×10^{15} ions/cm^2.

energy density. The simulation results have been extracted from heat flow equations that have been incorporated into the model described in Ref. 15. As we raise the laser energy density, and effectively increase the amount of energy deposited, the melt depth is increased. By utilizing such a chart we can select the melt depth and subsequently the junction depth with a high level of accuracy. In Fig. 4, the calculated liquid-solid interface velocity into and out of the solid for two different laser energy densities (615 and 900 mJ/cm^2) is presented. At higher laser energy densities, the temperature at the surface is raised and the thermal gradient between the liquid and solid phases is increased. The temperature difference between the two phases governs the melting process during irradiation, and the velocity of the interface into the solid is increased for higher laser energy densities. When the interface velocity falls to zero in the solid the maximum melt depth has been achieved, and the interface advances back toward the surface (designated as a negative velocity in the figure). It is observed that irrespective of the laser energy density, the interface advances toward the solid at a velocity of $\sim$2 m/s, (which is substantially slower than the melting process). The melt depth as a function of time (from when the pulse interacts with the solid) has been calculated and is shown in Fig. 5. Although for the simulation it is assumed that the laser energy is converted to heat instantaneously, there is a time interval before the phase change from solid to liquid actually occurs. It can be seen that the maximum melt depth is reached when the laser pulse (28 ns) has finished. For ELA at 615 mJ/cm^2, the maximum melt depth is achieved at 40 nm after 40 ns, and for ELA at 900 mJ/cm^2 the maximum melt depth is at 160 nm and achieved after 44 ns.

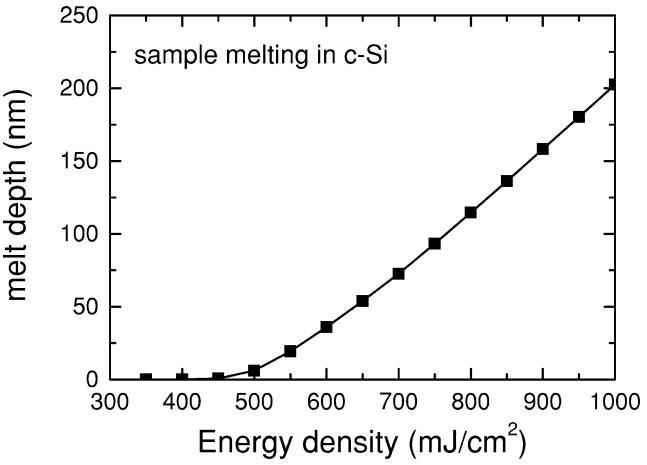

FIG. 3. The calculated melt depth induced in crystal Si during excimer laser irradiation as a function of the laser energy density.

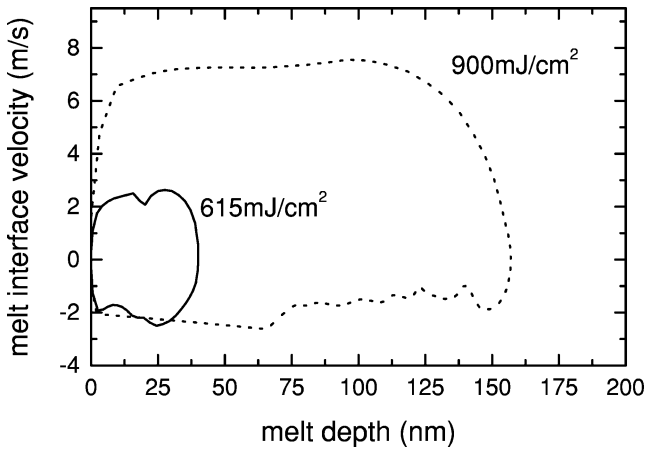

FIG. 4. The calculated liquid-solid interface velocity during melting (positive) and resolidification (negative) in Si during and immediately after laser irradiation at 615 and 900 mJ/cm^2.

B. Electrical activation, redistribution, and retention of B in Si during ELA

The electrical activation, redistribution, and retention of ULE-implanted B in Si (at doses ranging from 1×10^{14} to 5×10^{15} ions/cm^2) during ELA has been measured with SRP and SIMS for a range of laser annealing conditions. ELA has been performed at energy densities ranging from 575 to 900 mJ/cm^2 (inducing melt depths from 28 to 160 nm), and for different irradiation times (shot numbers from 1 to 50).

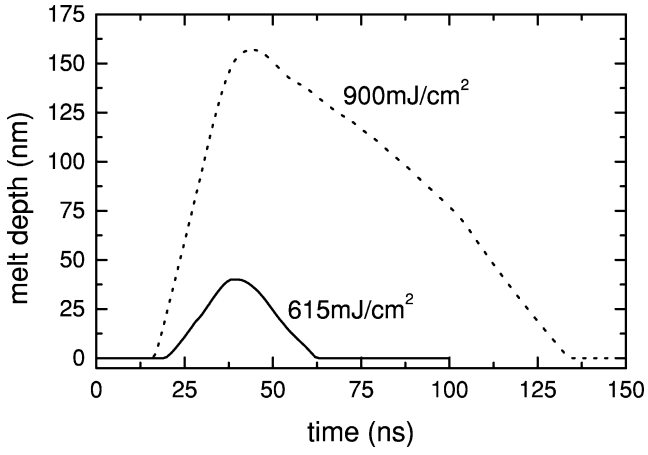

FIG. 5. The calculated melt depth induced in Si as a function of time for laser irradiation at 615 and 900 mJ/cm^2 (from when the pulse interacts with the solid).

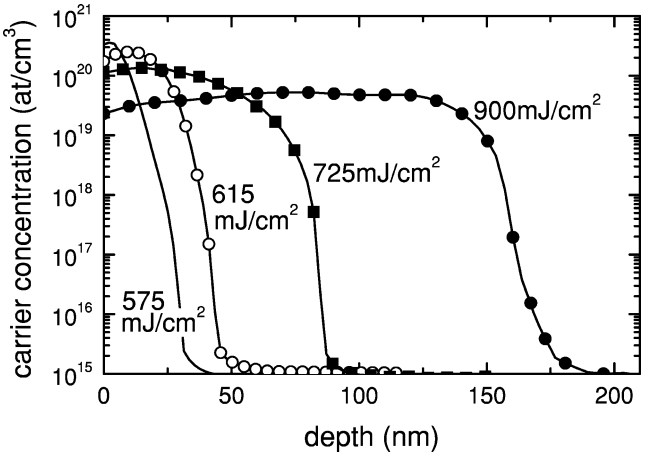

FIG. 6. Electrically active dopant profiles formed in Si following ten-pulse ELA (at 575, 615, 725, and 900 mJ/cm^2) of a 1-keV B implant (1×10^{15} ions/cm^2).

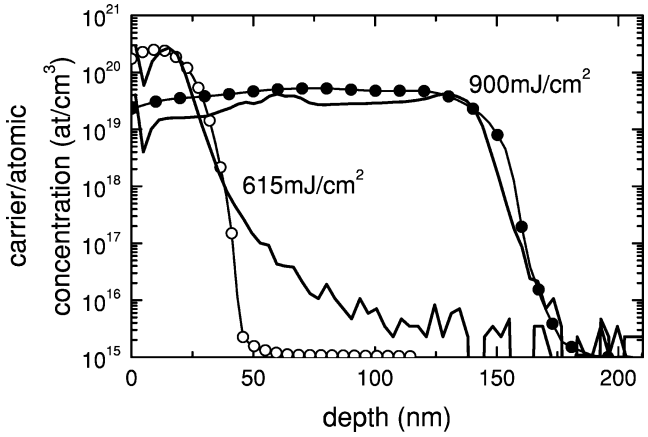

FIG. 7. Electrical (SRP, symbol) and chemical (SIMS, no symbol) dopant profiles formed in Si following ten-pulse ELA (at 615 and 900 mJ/cm^2) of a 1-keV B implant (1×10^{15} ions/cm^2).

The electrically active dopant profiles formed in Si following irradiation (for ten pulse shots) of samples implanted with 1-keV B to a dose of 1×10^{15} ions/cm^2 are presented in Fig. 6. The melt depth formed during irradiation is increased as the laser energy density is raised, and the dopant is subsequently redistributed over a larger range during melting. The area under the SRP profile is a direct measure of the activated dose (values given in Table I), and complete activation of the implanted dose was never achieved which suggests that either a fraction of the dopant remains inactive following ELA and/or is lost from the sample during ELA. The maximum carrier concentration is achieved following shallow melting. However, even though the carrier concentration is decreased when the dopant redistributes into the sample for deeper melting, the total activated dose is raised.

In order to compare the electrical and chemical dopant profiles, and hence determine the inactive fraction remaining in the solid following ELA, SRP in combination with SIMS analysis has been performed. It can be seen in Fig. 7 that within the melted depth, the chemical and electrical profiles (ignoring SIMS artifacts in the surface region) formed in Si following ELA are equal. We can observe that within the melted zone, all the dopant which is retained in the solid appears substitutional and is fully activated following recrystallisation from the liquid phase. For shallow melting, a small fraction of the implanted dopant remains at a position beyond the melted depth and as the sample is not melted in this region, no dopant activation is observed.

The electrically active dopant profile formed in Si following ELA (ten pulses) at a fixed energy density has been investigated for three implant doses (1×10^{14}, 1×10^{15}, and 5×10^{15} ions/cm^2). It can be seen in Fig. 8, that for a fixed melt depth [(a) 40 nm for 615 mJ/cm^2 and (b) 159 nm for 900 mJ/cm^2], the activated dose is raised as the implant dose is increased. For all three implant doses, a significant fraction of the dose is lost during ELA, the extent of which shows a dependence upon the dose implanted. The activation efficiency (dose activated/dose implanted into Si material) in samples implanted at 1×10^{14} and 1×10^{15} ions/cm^2 was a constant at ~61% following ELA at 615 mJ/cm^2. Following ELA at 615 mJ/cm^2 of a high dose implant (5×10^{15} ions/cm^2), although the total activated dose is increased in comparison to the lower doses, the efficiency is

TABLE I. The activation efficiency and sheet resistance of B layers formed in Si following ULE ion implantation and laser and/or thermal processing.

Implant dose (ions/cm^2)	Process condition (ELA or RTA)	Melt/diffusion depth (nm)	Active dose (ions/cm^2)/ activation efficiency (%)	Sheet resistance (Ω/sq)
1×10^{14}	ELA at 615 mJ/cm^2	41	5.4*E*13 (60%)	1600
1×10^{14}	ELA at 900 mJ/cm^2	159	6*E*13 (66%)	1200
1×10^{15}	**RTA** 1100 °C 30 s O_2	220	1.18*E*14 (13%)	460
1×10^{15}	ELA at 575 mJ/cm^2	28	3.1*E*14 (34%)	332
1×10^{15}	ELA at 615 mJ/cm^2	41	5.5*E*14 (61%)	215
1×10^{15}	ELA at 725 mJ/cm^2	83.5	6.2*E*14 (69%)	175
1×10^{15}	ELA at 900 mJ/cm^2	159	6.2*E*14 (69%)	210
5×10^{15}	ELA at 615 mJ/cm^2	41	1.6*E*15 (36%)	75
5×10^{15}	ELA at 900 mJ/cm^2	159	1.5*E*15 (69%)	34

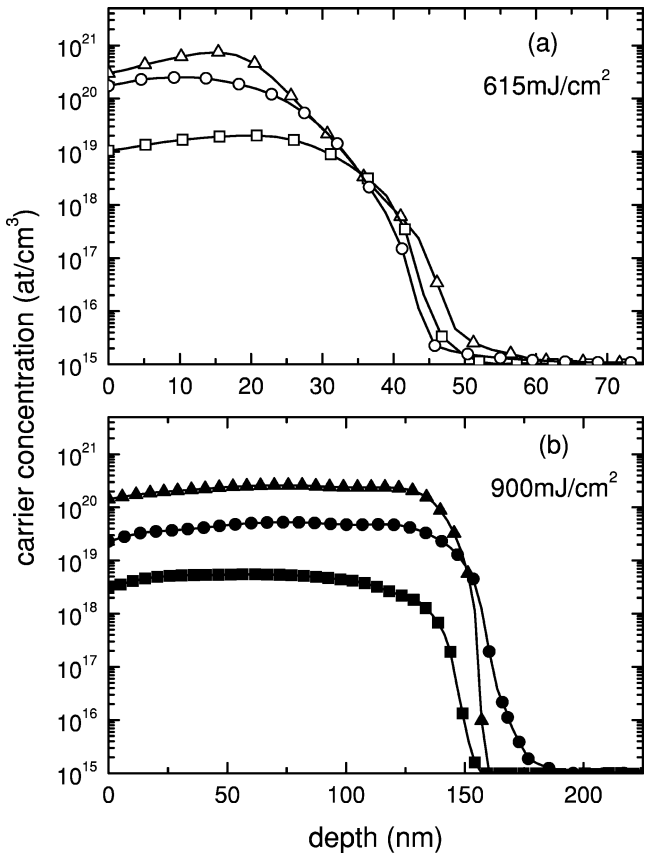

FIG. 8. Electrically active dopant profiles formed in Si following ten-pulse ELA at (a), 615 and (b), 900 mJ/cm^2 of samples implanted with 1-keV B at doses of 1×10^{14} (square), 1×10^{15} (circle), and 5×10^{15} ions/cm^2 (triangle).

reduced to 36%. For deeper melting (159 nm), the total activated dose was raised, and ~69% of the dopant that remained in Si material prior to ELA was activated irrespective of the dose implanted.

The level of dopant activation and redistribution as a function of the laser anneal time has been investigated and the active dopant profiles formed in Si following a series of laser pulses are shown in Fig. 9. It can be seen that for a fixed laser energy density [600 mJ/cm^2 (+\−10 mJ/cm^2)] and for a fixed implant dose (1×10^{15} ions/cm^2), the carrier concentration remained a constant as the total melt time was effectively increased. The redistribution depth appears to be slightly increased as the pulse number is raised. The increase could be caused by a fluctuation in laser energy density (+\−10 mJ/cm^2), and/or solid phase diffusion in the heated region just beyond the maximum melt depth position. However, if we consider the fraction of the implanted dopant which is lost from the sample during ELA, the profiles presented in Fig. 9 clearly indicate that the major dopant loss mechanism occurs during the first pulse only. It is also evident that the dopant is able to fully redistribute to the melt depth during the initial pulse.

A HRTEM analysis has been performed upon a sample implanted with 1-keV B to a dose of 1×10^{15} ions/cm^2 and laser annealed at 615 mJ/cm^2. The HRTEM image shown in Fig. 10, taken from the surface region, shows that the crystal

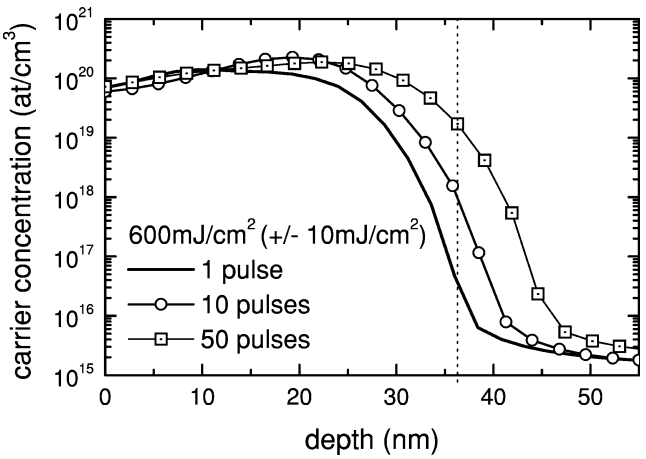

FIG. 9. Electrically active dopant profiles formed in Si following ELA at 600 mJ/cm^2 (+/−10 mJ/cm^2) of a 1-keV B implant (1×10^{15} ions/cm^2) for a series of laser pulses (1, 10, and 50).

structure is fully restored following ELA. The oxide layer, which cannot be identified at high magnification, but has been identified (and measured as ~3 nm) at lower magnification, appears to be in the same state as it did prior to ELA and is expected to remain solid during irradiation. The laser annealing process appears to form highly crystalline material following regrowth from the melt phase, and no defect region at the liquid-crystal interface position (40 nm) has been identified at low magnification (results not shown). The dark band observed at ~5 nm is not caused by crystal irregularity but by a change in the sample thickness.

The dopant activation during ELA is of vital importance and directly affects the sheet resistance of the processed layer. Table I reports the sheet resistance values measured from the laser annealed samples shown in Figs. 6 and 8. As a reference, the sheet resistance and activated dose obtained from a conventional RTA process is presented. In compari-

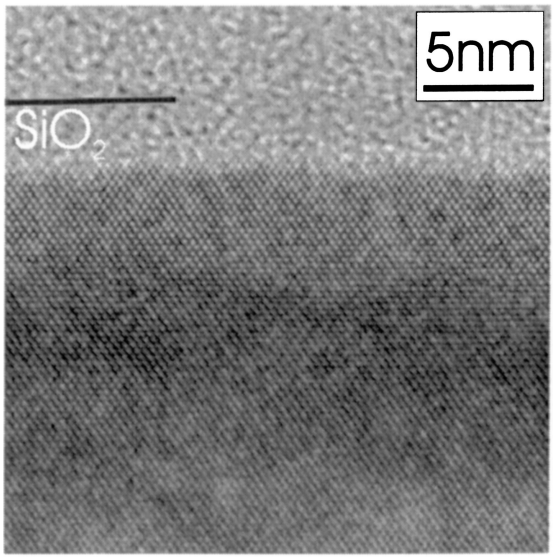

FIG. 10. HRTEM of the near-surface region of a sample implanted with 1-keV B to a dose of 1×10^{15} ions/cm^2 and ELA at 615 mJ/cm^2.

son to the sheet resistance and junction depth formed in a sample of the same implant dose through conventional RTA process, the level of electrical activation achievable with ELA make it appear a much more viable procedure for the fabrication of future electronic devices. As in RTA processes, a slight trade off is required, as a lower sheet resistance was achieved for deeper melting. However, through a knowledge of the dopant activation (retention) for a specific melt depth, the implant dose can be chosen to give the desired sheet resistance, allowing much more control over device fabrication.

IV. DISCUSSION

Ultrashallow dopant profiles with a high electrical activation have been formed in Si following ULE B-ion implantation and ELA. It has been shown that dopant loss occurred during the laser annealing process. The extent of the dopant loss depended upon the redistribution depth and it has been demonstrated that the majority of the dopant loss occurred during the first laser pulse only. It was assumed that the presence of substitutional B and the change in the Si band gap, following the initial laser pulse, have a negligible effect upon the absorption properties of the laser pulse (at an energy of 4 eV) during subsequent irradiation. The as-implanted amorphous surface damage layer was regrown prior to ELA when the sample was maintained at 450 °C (TEM results not shown), and hence irradiation was performed upon crystalline material. Therefore, the melting process that occurs during pulse one is expected to be similar to the melting process that occurs during subsequent pulses.

However, although the melting process is expected to be similar for each pulse, the B redistribution process was expected to change as a function of the pulse number. Prior to the initial pulse, the as-implanted dopant profile remained in a Gaussian form in the near-surface region of the sample. Prior to the second pulse, the dopant profile was deeper in depth and lower in atomic concentration with respect to the as-implanted profile. In order to explain the dopant behavior during melting and regrowth, a model considering the melt depth, melt time and interface velocity (taking the values from Figs. 3–5), has been developed. The model considers standard diffusion equations with diffusivity coefficients D_l D_s, and D_{ox} in the liquid Si, solid Si, and solid SiO_2 materials' respectively. During the ELA process the dopant density C evolves according to the equation

$$\frac{\partial C}{\partial t} = \frac{\partial}{\partial z}\left(D(z)\frac{\partial C}{\partial z}\right), \tag{1}$$

where

$$D(z) = \begin{cases} D_{ox} & \text{if } z_{surf} < z < z_{ox} \\ D_l & \text{if } z_{ox} < z < z_{im} \\ D_s & \text{if } z > z_{int} \end{cases}, \tag{2}$$

and z_{surf}, z_{ox}, and z_{int} are the free surface, the SiO_2-Si interface, and the liquid-solid interface positions, respectively. Note that z_{surf} and z_{ox} are fixed, while we assume an ideal motion of z_{int} with constant speeds during melting and regrowth (estimated from the thermal simulations), a smooth inversion of the motion in the region where the maximum melt depth is reached, and a smooth deceleration when approaching the surface. These assumptions seem a reliable approximation of the results of thermal field simulation (see Fig. 4).

We consider the boundary conditions

$$D(z)\frac{\partial C}{\partial z}\bigg|_{z=z_{int}}^{\pm} = \pm \nu_{int}(k_{segr}-1)C$$

at the interface poisitions, (3)

$$D(z)\frac{\partial C}{\partial z}\bigg|_{z=z_{surf}} = -R(C-C_{eq})$$

at the free surface positions, (4)

where v_{int} is the interface velocity, k_{segr} the segregation coefficient, R the surface recombination coefficient, and C_{eq} the surface equilibrium density. The $-(+)$ sign indicates the left (right) derivative in the liquid (solid) region. At high implantation doses, the dopant atomic density may approach the thermodynamic limit. This effect has been incorporated into the model and, a reduced value of k_{segr} is considered at high dopant densities. We assume the following phenomenological dependence of k_{segr} on the dopant density at the liquid-solid interface,

$$k_{segr}[C^-(z_{int})] = C_{crit}/C^-(z_{int}) \times \tanh[C^-(z_{int})/C_{crit}], \tag{5}$$

where the model parameter C_{crit} is the critical dopant concentration at the transition phase when the dopant incorporation process becomes restricted with respect to the case for lower doses. According to relation (5), k_{segr} tends to the limit ($k_{segr} \approx 1$ (Ref. 16)) for the low-density case, while it scales as $C_{crit}/C(z_{int})$ when $C(z_{int}) \gg C_{crit}$.

For the simulation results shown in Fig. 11, the average melt depth was assumed to be 33 nm which relates to a laser energy density of 600 mJ/cm^2, and allows comparison with the experimental SRP results presented in Fig. 9. In order to take into account the small fluctuation in laser energy density (± 10 mJ/cm^2) between laser pulses, we consider that the melt depth reached after each pulse can vary randomly around the average value with a gaussian distribution, having a variance $\sigma_{depth} = 4$ nm. Note that this procedure leads to a variation of the resulting profile depth for a fixed laser energy density, which in turn has been evidenced in the experimental profiles. Finally, as stated above, a smooth variation of the interface speed v_{nt} during regrowth (from zero to ~ 2 m/s at the maximum melt depth and from ~ 2 m/s to zero at the surface region (Fig. 4) has been considered in the simulation.

The initial profile prior to ELA was taken as the SIMS as-implanted profile shown in Fig. 2 (with the anomalous surface peak removed prior to calculations). When considering B diffusion coefficients of $D_l = 1 \times 10^{-4}$ cm^2 s,[7] $D_s = 3 \times 10^{-8}$ cm^2/s, and $D_{ox} = 1 \times 10^{-12}$ cm^2 s (estimated at a temperature just below the melting temperature of Si, using the values given in (Ref. 17), $C_{crit} = 8 \times 10^{20}$ cm^{-3} (see the discussion below), and negligible surface recombination [the

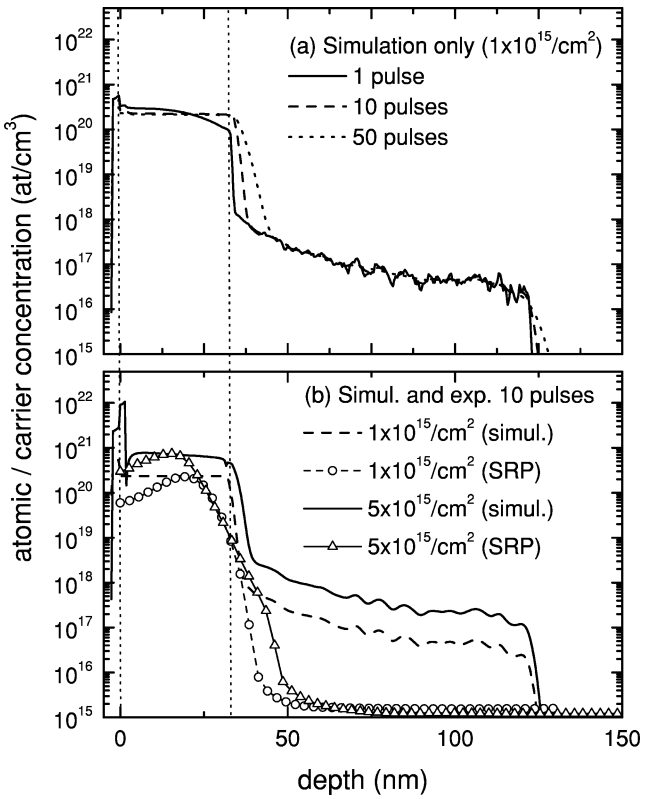

FIG. 11. Simulated and experimental (section *b* only) dopant profiles formed in Si following a 1-keV B implant and ELA at 600 mJ/cm^2 as a function of the pulse number (a), and the implant dose (b) (the oxide layer is above the Si surface position, which is at zero on the depth scale).

$(R/D)^{-1} \gg$ profile feature size], the dopant profile develops into the sample (and into the solid oxide) as shown in Fig. 11(a). The main profile characteristics were governed by the diffusivity in liquid Si, the segregation coefficient and the surface recombination coefficient. As the dopant profile is initially at high concentration close to the surface oxide layer, a major fraction of the ''lost'' dopant redistributed into the solid oxide during the first pulse only. For subsequent pulses, the dopant profile remained at a lower atomic concentration and significantly less dopant was transferred from the Si into the SiO_2 layer.

For simulation purposes, the dopant remained trapped in the solid oxide during ELA, and was effectively lost from the Si region. We are unable to determine experimentally whether or not the dopant remained as a stable layer in the surface oxide or was lost through evaporation processes. No evidence of dopant precipitation was observed in the surface oxide with HRTEM, which suggests that the dopant redistributed into the surface region during melting was lost through out diffusion. Beyond the maximum melt depth position, solid phase diffusion occurred and the dopant profile broadened as the pulse number was increased. As the simulation considers the complete atomic concentration, the inactive dopant that remains beyond the melted depth (as identified in Fig. 7) can be observed in Fig. 11.

For high dose implantation (5×10^{15} ions/cm^2) and shallow melting (615 mJ/cm^2), when the dopant redistribution

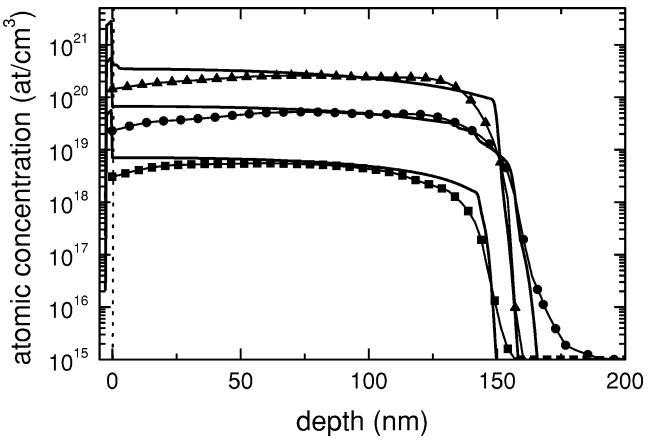

FIG. 12. Simulated (solid line) and experimental (SRP, symbols) dopant profiles formed in Si following a 1-keV B implant (dose 1×10^{14} (square) 1×10^{15} (circle), and 5×10^{15} (triangle) ions/cm^2, and ELA at 900 mJ/cm^2 for ten pulses.

was restricted within a melt depth of 40 nm, the extent of the dopant loss was enhanced and did not follow the same trends as for the lower concentrations. The maximum atomic concentration formed in this sample was ~2%, which is at a sufficient level so that dopant trapping is limited during regrowth. In fact, the activation efficiency in this sample is considerably reduced with respect to the low dose, shallow melting and the high dose, deep melting cases (see Table I), which suggests that a fraction of the dopant was lost (pushed out) at the advancing interface during regrowth, and that the dopant trapping mechanism in this sample was impeded. The comparison between the simulation and experimental results for this sample [see Fig. 11(b)], shows that the reduction in the activation efficiency can be predicted in our model when using a value of $C_{crit}\sim8\times10^{20}$ cm^{-3} in expression (5). The simulation result shows a segregation peak in the surface region.

We also performed a large set of trial simulations by changing the input parameters over a wide range of values, including a segregation coefficient of less than unity at low atomic concentration, and a surface recombination coefficient greater than zero. However, the results obtained and shown in Figs. 11 and 12, show the best agreement with the experimental data when no segregation at low density [i.e., $k_{segr}\approx1$ when $C-(z_{int})\ll C_{crit})$] and negligible surface recombination [$(R/D)^{-1}$ much larger than the profile feature size] are assumed.

It has been shown that when the thermodynamic limit was not reached during dopant redistribution in the melt phase, the activation efficiency (dose activated and dose implanted into Si material) was a constant for a fixed melt depth irrespective of the implant dose. The fact that the activation efficiency was a constant for different implant doses, suggests that the as-implanted chemical concentration gradient and the absolute atomic concentration level did not directly affect the fraction of the implanted dose lost. As the simulation results suggest in Fig. 12, the dopant profile formed in Si after ELA (when below the thermodynamic limit) is an intrinsic property of the laser anneal process, and is governed

by the diffusion equation and the melt depth. Indeed, since the laser anneal process fixes the dimension of the melted box (i.e., the region in which the retained dopant redistributes) and other geometrical conditions are also fixed, we do not expect any relevant dependence of the profile shape upon the absolute dose value. An intrinsic dose dependence would only arise if the diffusion mechanism was influenced by a dose level limit. However, for an atomic concentration level below the thermodynamic limit, we demonstrate that the experimental data can be reliably fitted using a model which can be rescaled with the implant dose only (in this case we chose $\sigma_{\text{depth}}=14$ nm). It has been demonstrated that the dopant loss depended upon the laser energy density. For a higher laser energy density annealing the dopant was redistributed over a deeper range, and although the temperature at the surface is expected to be higher, less dopant was lost from the solid. The dopant redistributes into and out of the solid according to the melted depth, as shown experimentally in Fig. 6 and theoretically in Figs. 11 and 12. For deeper melting, as the interface velocity sweeps into the solid, less dopant is redistributed towards, and contained close to, the surface and as a result less dopant is lost from the sample.

V. CONCLUSION

The B activation, redistribution, and retention in Si during ELA has been investigated as a function of the laser condition and the implanted dose. Ultrashallow (<100 nm), electrically active B profiles were successfully formed in Si following ULE ion implantation and ELA. A fraction of the implanted dopant was lost from the sample during laser annealing through redistribution into the surface region. Major dopant loss occurred during the initial laser pulse only, the extent of which was shown to depend upon the melt depth. The dopant that was retained in the solid was fully activated, and the material formed after liquid phase epitaxial regrowth was highly crystalline. At an atomic concentration below the thermodynamic limit, the activation efficiency was a constant irrespective of dose implanted for a fixed melt depth. When dopant concentrations were formed above the thermodynamic limit the activation efficiency was reduced for a given melt depth.

A theoretical model that considers dopant redistribution during melting and regrowth has been developed. The model has been used to explain the dopant behavior when the dopant atomic concentration at the liquid-solid interface is low or comparable to the thermodynamic limit. The theoretical results have been compared to the experimental observations. The trends observed experimentally have been successfully confirmed by the simulation profiles when assuming a phenomenological expression for the segregation coefficient (interpolating from the low-density limit value $k_{\text{segr}}\approx 1$ up to the thermodynamic limit), and negligible surface recombination during melting and regrowth.

ACKNOWLEDGMENTS

The authors would like to thank Applied Materials (UK) for the implants, Emanuele Rimini for many helpful discussions, Francesco Mammoliti for support with the electrical measurements, Enrico Napolitani for the profile reported in Fig. 2 and Patrick Leveque and J. S. Christensen for the SIMS profiles reported in Fig. 7. The research was partially funded by EU project No. FMRX-CT98-0208, ENDEASD.

*Electronic mail: sw349@eng.cam.ac.uk

[1] M. A. Foad and D. Jennings, Semicond. Sci. Technol. **41**, 43 (1998).
[2] A. H. Al-Bayati, K. G. Orrman-Rossiter, J. A. van den Berg, and D. G. Armour, Surf. Sci. **241**, 91 (1991).
[3] P. A. Stolk, H-J Gossmann, D. J. Eaglesham, D. C. Jacobson, C. S. Rafferty, G. H. Gilmer, M. Jaraíz, J. M. Poate, H. S. Luftman, and T. E. Haynes, J. Appl. Phys. **81**, 6031 (1997).
[4] R. F. Wood, J. R. Kirkpatrick, and G. E. Giles, Phys. Rev. B **23**, 5555 (1981).
[5] S. Whelan, V. Privitera, M. Italia, G. Mannino, C. Bongiorno, C. Spinella, G. Fortunato, L. Mariucci, M. Stanizzi, and A. Mittiga, J. Vac. Sci. Technol. B **20**, 644 (2002).
[6] E. Rimini, in *Surface Modification and Alloying by Laser, Ion and Electron Beams*, edited by J. M. Poate, G. Foti, and D. Jacobsen (Plenum, New York, 1983), Chap. 2, p. 26.
[7] V. Privitera, C. Spinella, G. Fortunato, and L. Mariucci, Appl. Phys. Lett. **77**, 552 (2000).
[8] K. A. Jackson, in *Surface Modification and Alloying by Laser, Ion and Electron Beams* (Ref. 6), Chap. 3, p. 59.
[9] A. G. Cullis, H. C. Webber, J. M. Poate, and A. L. Simons, Appl. Phys. Lett. **36**, 320 (1980).
[10] B. C. Larson, C. W. White, and B. R. Appleton, Appl. Phys. Lett. **32**, 801 (1978).
[11] J. W. Cahn, S. R. Coriell, and W. J. Boettinger, in *Laser and Electron Beam Processing of Materials*, edited by C. W. White and P. S. Peercy (Academic, New York, 1980), p. 89.
[12] V. Privitera, E. Schroer, F. Priolo, E. Napolitani, and A. Camera, J. Appl. Phys. **88**, 1299 (2000).
[13] T. Clarysse, W. Vandervorst, and M. Pawlik, J. Vac. Sci. Technol. B **14**, 390 (1996).
[14] J. F. Ziegler, *Handbook of Ion Implantation Technology* (North-Holland, Amsterdam, 1992).
[15] G. G. Bentini, M. Bianconi, and C. Summonte, Appl. Phys. A: Solids Surf. **45**, 317 (1988).
[16] C. W. White, D. M. Zehner, S. U. Campisano and A. Cullis, in *Surface Modification and Alloying by Laser, Ion and Electron Beams* (Ref. 6), Chap. 4, p. 90.
[17] M. Ghezzo and D. M. Brown, J. Electrochem. Soc. **120**, 146 (1973).